Papers in the Earth and Atmospheric Sciences

Earth and Atmospheric Sciences, Department of

2017

Dynamics of Cloud-Top Generating Cells in Winter Cyclones. Part III: Shear and Convective Organization

Jason M. Keeler
University of Nebraska–Lincoln

Robert M. Rauber
University of Illinois at Urbana–Champaign

Brian F. Jewett
University of Illinois at Urbana–Champaign

Greg M. McFarquhar
University of Illinois at Urbana–Champaign

Roy M. Rasmussen
National Center for Atmospheric Research, Boulder

See next page for additional authors

Authors

Jason M. Keeler, Robert M. Rauber, Brian F. Jewett, Greg M. McFarquhar, Roy M. Rasmussen, Lulin Xue, Changhai Liu, and Gregory Thompson

Dynamics of Cloud-Top Generating Cells in Winter Cyclones. Part III: Shear and Convective Organization

JASON M. KEELER

Department of Earth and Atmospheric Sciences, University of Nebraska–Lincoln, Lincoln, Nebraska

ROBERT M. RAUBER, BRIAN F. JEWETT, AND GREG M. MCFARQUHAR

Department of Atmospheric Sciences, University of Illinois at Urbana–Champaign, Urbana, Illinois

ROY M. RASMUSSEN, LULIN XUE, CHANGHAI LIU, AND GREGORY THOMPSON

Research Applications Laboratory, National Center for Atmospheric Research, Boulder, Colorado

ABSTRACT

Cloud-top generating cells (GCs) are a common feature atop stratiform clouds within the comma head of winter cyclones. The dynamics of cloud-top GCs are investigated using very high-resolution idealized WRF Model simulations to examine the role of shear in modulating the structure and intensity of GCs. Simulations were run for the same combinations of radiative forcing and instability as in Part II of this series, but with six different shear profiles ranging from 0 to $10\,\mathrm{m\,s^{-1}\,km^{-1}}$ within the layer encompassing the GCs.

The primary role of shear was to modulate the organization of GCs, which organized as closed convective cells in simulations with radiative forcing and no shear. In simulations with shear and radiative forcing, GCs organized in linear streets parallel to the wind. No GCs developed in the initially stable simulations with no radiative forcing. In the initially unstable and neutral simulations with no radiative forcing or shear, GCs were exceptionally weak, with no clear organization. In moderate-shear ($\Delta u/\Delta z = 2, 4\,\mathrm{m\,s^{-1}\,km^{-1}}$) simulations with no radiative forcing, linear organization of the weak cells was apparent, but this organization was less coherent in simulations with high shear ($\Delta u/\Delta z = 6, 8, 10\,\mathrm{m\,s^{-1}\,km^{-1}}$). The intensity of the updrafts was primarily related to the mode of radiative forcing but was modulated by shear. The more intense GCs in nighttime simulations were either associated with no shear (closed convective cells) or strong shear (linear streets). Updrafts within GCs under conditions with radiative forcing were typically $\sim$1–2 $\mathrm{m\,s^{-1}}$ with maximum values $< 4\,\mathrm{m\,s^{-1}}$.

1. Introduction

The term "generating cell" describes a small region of locally high radar reflectivity at cloud top from which an enhanced reflectivity trail characteristic of falling snow particles originates (American Meteorological Society 2016). Generating cells are typically characterized by updrafts of 0.75–3.00 $\mathrm{m\,s^{-1}}$ in the upper 1–2 km of clouds that are otherwise stratiform in nature (Wexler 1955; Douglas et al. 1957; Wexler and Atlas 1959; Carbone and Bohne 1975; Rosenow et al. 2014; Kumjian et al. 2014). Cloud-top generating cells (GCs) have been observed with vertically pointing radars since the 1950s (Marshall 1953). Comprehensive reviews of the literature of

the last six decades related to GCs and their role in the precipitation process in the comma-head region of extratropical cyclones appear in recent works by Rosenow et al. (2014), Kumjian et al. (2014), Rauber et al. (2014a,b, 2015), Plummer et al. (2014, 2015), and Keeler et al. (2016a, hereafter Part I, 2016b, hereafter Part II).

In Part I, cloud-top GCs were simulated in an idealized environment representative of the comma-head region of the 14–15 February 2010 cyclone observed during the Profiling of Winter Storms (PLOWS) field campaign (Rauber et al. 2014a). Observations of this storm (Rosenow et al. 2014; Plummer et al. 2014, 2015) showed 1.5–2.0-km-deep GCs atop a deep nimbostratus cloud. Fall streaks emanated from the GCs and merged into bands as they approached the surface. In Part I, the influence of radiative forcing and latent heating on the

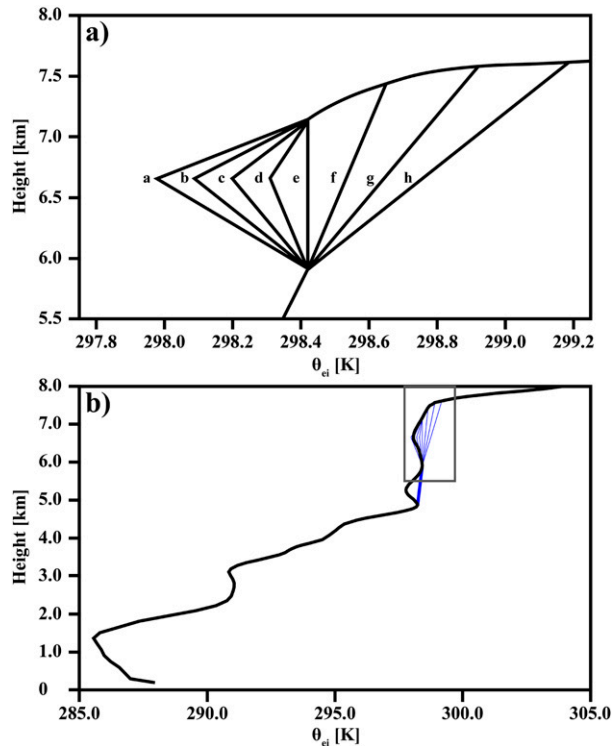*Corresponding author*: Jason M. Keeler, jkeeler9@unl.edu

FIG. 1. (a) Equivalent potential temperature with respect to ice θ_{ei} (K) for each stability profile (labeled a–h) displayed between 5.5- and 8.0-km altitude. (b) Profile of θ_{ei} (K) for 0 to 8 km from Part II (black line), with modifications to profiles shown in (a) shown in blue. The extent of (a) is indicated by the gray-line rectangle.

development and maintenance of the GCs was examined using high-resolution idealized Weather Research and Forecasting (WRF) Model simulations with initial wind and thermodynamic conditions representative of the vertical structure of the comma-head region of this cyclone where GCs were observed. In the simulations in Part I, GCs developed because of the presence of weak potential instability[1] in the cloud-top region (5.9–6.7 km, $\Delta\theta_{ei}/\Delta z = -0.40 \, \mathrm{K \, km^{-1}}$). Simulations were performed for nighttime (longwave forcing only), daytime (longwave and shortwave forcing), and no-radiation conditions. Longwave radiative cooling at cloud top was found to be critical to the maintenance of the GCs. GCs regenerated in simulations with radiative forcing and were strongest in the nighttime simulations. The GCs were found not to persist when radiation was not included, demonstrating that radiative forcing was critical to GC maintenance under the thermodynamic and vertical wind shear conditions in this cyclone.
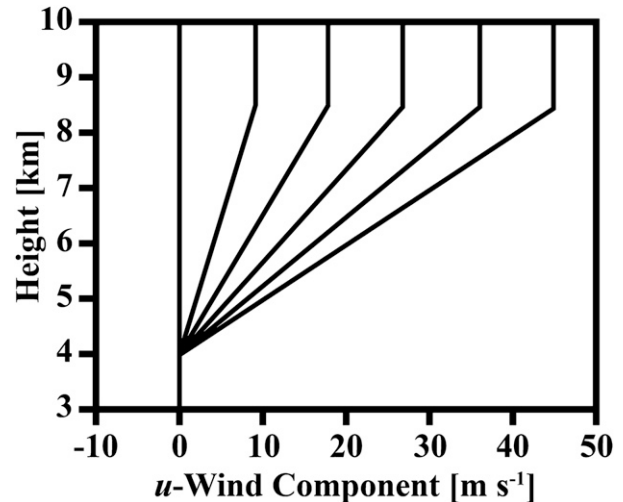

FIG. 2. Vertical profiles of the u component of wind for the idealized vertical wind shear simulations. The base-state u and v components of the wind are set at $0 \, \mathrm{m \, s^{-1}}$ for all simulations.

In Part II, the sensitivity of the GCs to upper-tropospheric stability was assessed under conditions of different radiative forcing using the same model framework. The wind profile in these simulations was the same as in Part I. Input model fields near cloud top were modified from the Part I base sounding so that the GCs could be investigated under potentially unstable ($\Delta\theta_{ei}/\Delta z = -0.53$, -0.40, -0.27, and $-0.13 \, \mathrm{K \, km^{-1}}$), neutral ($\Delta\theta_{ei}/\Delta z = 0 \, \mathrm{K \, km^{-1}}$), and stable ($\Delta\theta_{ei}/\Delta z = 0.15$, 0.30, and $0.45 \, \mathrm{K \, km^{-1}}$) initial conditions, again with nighttime, daytime, and no radiative forcing. It was found that GCs developed in the presence of cloud-top potential instability and persisted when radiative forcing was present. Even under neutral and stable cloud-top conditions, radiative forcing was found to destabilize the cloud top so that GCs could develop, providing a physical explanation for the ubiquity of GCs seen in field observations. GCs consisted of stronger updrafts and higher ice precipitation mixing ratios[2] under nighttime conditions, when destabilization due to longwave cooling was not offset by shortwave heating. GCs did not develop in the absence of radiative forcing unless cloud-top potential instability was present. In the case when potential instability was present, the GCs did not persist after the potential instability was exhausted.

---

[1] Potential instability is defined herein as an atmospheric state in which equivalent potential temperature with respect to ice θ_{ei} decreases with altitude.

[2] In this series, ice precipitation mixing ratio q_i is defined as the sum of the cloud-ice and snow mixing ratios. The graupel mixing ratio is not included since the temperature at the GC level is colder than $-40°C$ in these simulations.

TABLE 1. Moist-ice bulk Richardson number Ri_{Bmi} calculated over the 5.9–6.7-km layer at $t = 0$ min for simulations with stability and shear profiles shown in Figs. 1 and 2, respectively. Positive values of $Ri_{Bmi} < 0.25$ (consistent with shear instability) are in bold. For shear $= 0$, $\lim_{\text{Shear} \to 0} (Ri_{Bmi})$ is shown.

	Stability profile							
Shear	a	b	c	d	e	f	g	h
0	$-\infty$	$-\infty$	$-\infty$	$-\infty$	0	∞	∞	∞
2	-4.16	-3.14	-2.12	-1.02	0	1.18	2.35	3.53
4	-1.04	-0.78	-0.53	-0.25	0	0.29	0.59	0.88
6	-0.46	-0.35	-0.24	-0.11	0	**0.13**	0.26	0.39
8	-0.26	-0.20	-0.13	-0.06	0	**0.07**	**0.15**	**0.22**
10	-0.17	-0.13	-0.08	-0.04	0	**0.05**	**0.09**	**0.14**

A common feature of Wyoming Cloud Radar (WCR) observations from PLOWS was the persistence of fall streaks emanating from the GCs. Fall streaks were either identifiable from GC bases to the surface or were advected out of the time–height plane sampled by the radar when winds had a component across the plane (Rosenow et al. 2014; Rauber et al. 2014a,b, 2015; Plummer et al. 2015). While the altitude of GC bases varied slightly within the comma head of a given cyclone or more substantially between cyclones observed in PLOWS, typical GC bases ranged from 5 to 8 km AGL. Assuming a mean ice crystal or aggregate terminal velocity of $\sim 1 \, \text{m s}^{-1}$ [see Rosenow et al. (2014) and references therein, their Fig. 2], persistence of spatially continuous fall streaks from GC bases to the surface would require continuous generation of precipitation over a ~ 1.4–2.2-h period. In fact, Langleben (1956) tracked individual GCs for 1–2 h using radar data. Considering that a single updraft pulse with vertical velocity $w = 1$–$2 \, \text{m s}^{-1}$ would traverse the typical 1.5-km depth of a GC in 0.2–0.4 h, the PLOWS observations and those by Langleben (1956) suggest that coherent updrafts must be maintained over a long time period. Vertical wind shear represents a potential mechanism to organize updrafts and increase their longevity.

This paper builds on Parts I and II of this series by examining the role of shear in both the organization and intensity of updrafts associated with GCs. As with Part II, the structure and evolution of GCs under conditions of nighttime, daytime, and no radiative forcing are examined, but the additional factor of vertical wind shear
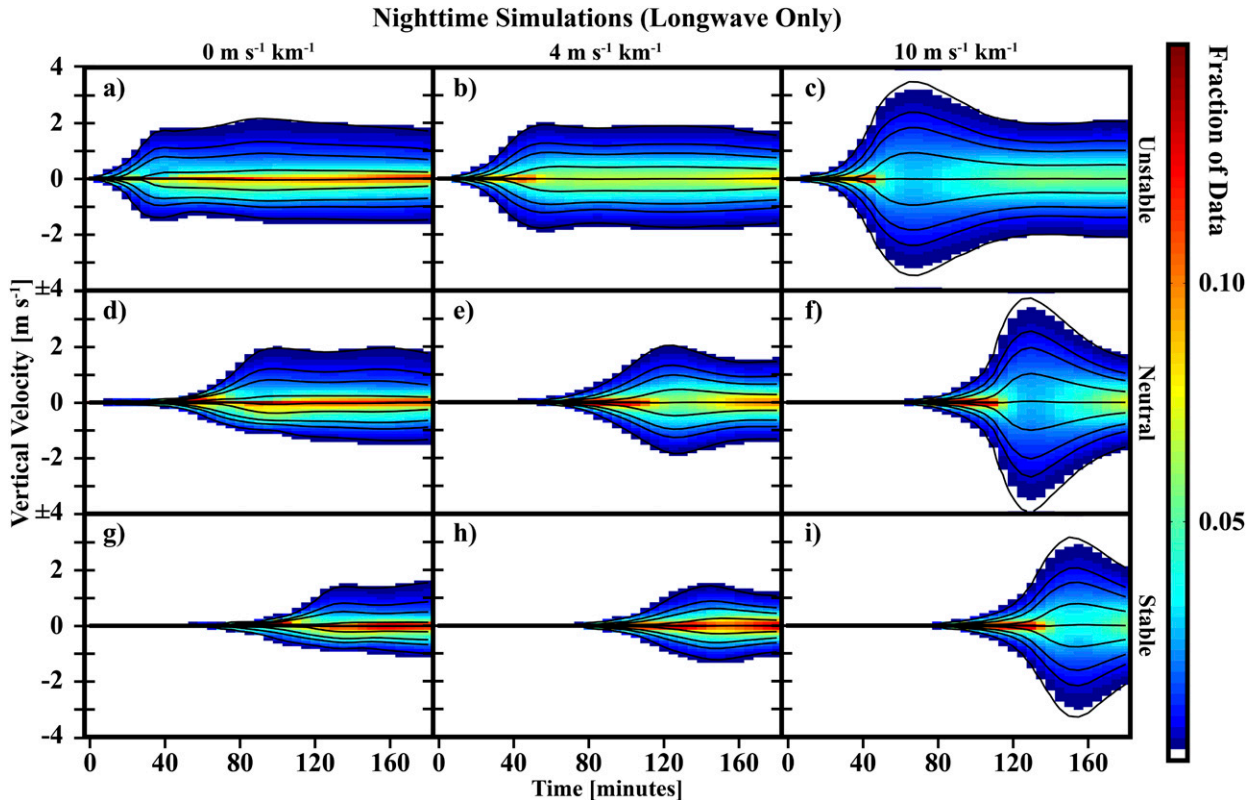
FIG. 3. CFTD analysis of the vertical air velocity data at the GC level (6–8 km) every 5 min with $0.1 \, \text{m s}^{-1}$ bin width for the nighttime simulations. Rows correspond to (top to bottom) stability profiles a, e, and h (see Fig. 1), and columns correspond to u shear of (left to right) 0, 4, and $10 \, \text{m s}^{-1} \, \text{km}^{-1}$ (see Fig. 2). Contours in individual panels show the 99th, 95th, 90th, 75th, 50th, 25th, 10th, 5th, and 1st percentiles of w.

FIG. 4. As in Fig. 3, but for the daytime simulations.

is considered. Six wind shear profiles are combined with the three radiative forcing modes and eight stability profiles used in Part II, yielding a total of 144 separate simulations investigating the structure, organization, and intensity of GCs.

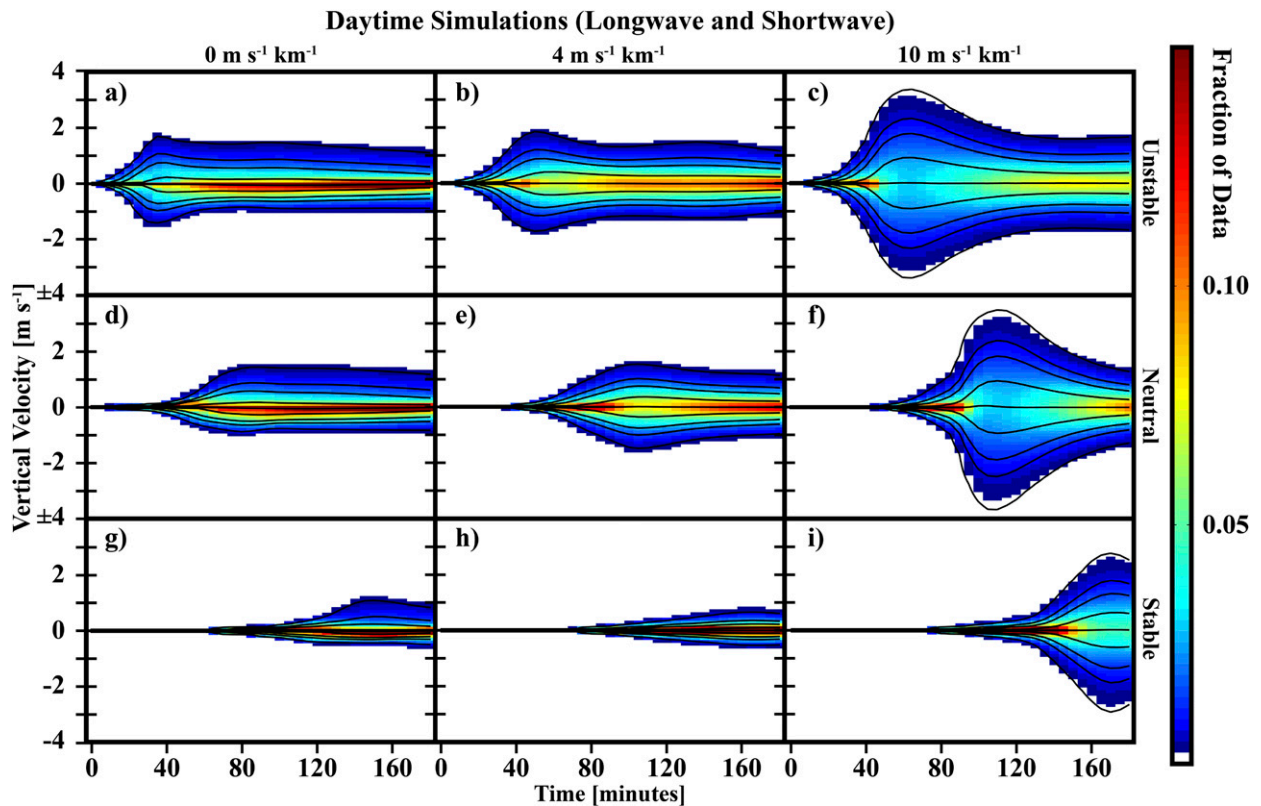In addition to buoyancy-driven instabilities discussed in Parts I and II, the inclusion of shear as a variable in this paper necessitates discussion of shear-driven instability [i.e., Kelvin–Helmholtz (K–H)]. The classic papers on shear instability focus on organization of convection in a theoretical, dry atmosphere (Case 1960; Dyson 1960; Kuo 1963; Asai 1970a,b). K–H instability is assessed using the bulk Richardson number Ri_B. When $0 > Ri_B > 0.25$, convective overturning is favored in the form of K–H waves. However, linear cloud streets are also possible for $0 > Ri_B > -2$ (Kuo 1963). In this paper, we assess the presence of K–H instability using the moist-ice bulk Richardson number as follows [adapted from Markowski and Richardson (2010) and Cunningham and Yuter (2014)]:

$$Ri_{Bmi} = \frac{\left(g/\Theta_{ei}\right)\left(\Gamma_{mi}/\Gamma_d\right)\left(\Delta\theta_{ei}/\Delta z\right)}{\left(\Delta u/\Delta z\right)^2 + \left(\Delta v/\Delta z\right)^2},$$

where g is the acceleration due to gravity, θ_{ei} is the equivalent potential temperature with respect to ice, Θ_{ei} is the mean θ_{ei} for the layer under consideration, Γ_{mi} is the moist-ice adiabatic lapse rate, Γ_d is the dry adiabatic lapse rate, u and v are the west–east and south–north components of the wind, and Δz is the depth of the layer for which Ri_{Bmi} is calculated.

K–H billows have been observed in cold season precipitation systems recently, including within a cold-frontal layer in Oklahoma (Houser and Bluestein 2011) and in a ''quasi-moist-neutral'' layer embedded within a cloud layer over complex terrain in Wyoming (Geerts and Miao 2010). Waves near cloud top were also recently observed using the High-Performance Instrumented Airborne Platform for Environmental Research (HIAPER) Cloud Radar in a Nor'easter (Rauber et al. 2017), although analysis was not performed to assess the role of shear in their development.

2. Idealized simulation methodology

a. Initial conditions

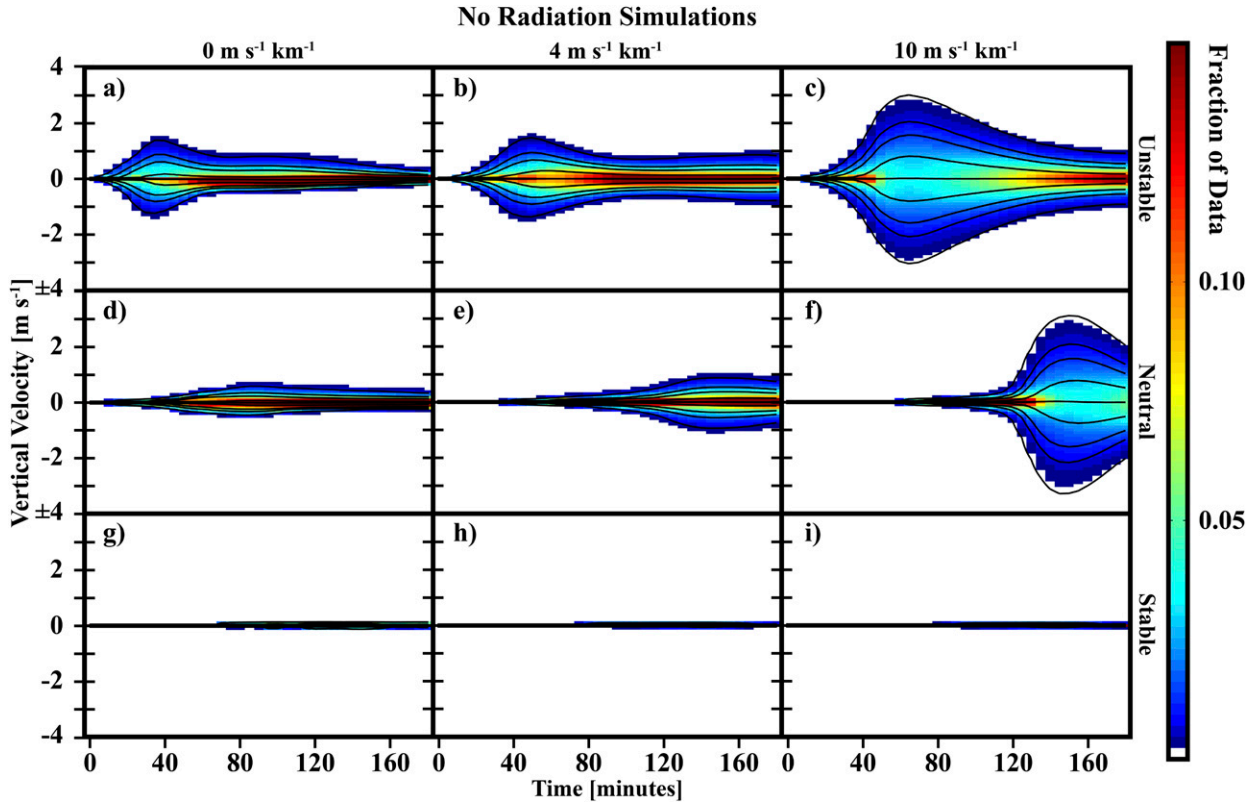A suite of idealized simulations was run to assess the role of vertical wind shear on the development,

FIG. 5. As in Fig. 3, but for the no-radiation simulations.

maintenance, and organization of GCs. In Parts I and II, initial conditions for idealized simulations of GCs consisted of a profile of potential temperature, water vapor mixing ratio, and horizontal wind components (θ, q_v, u, and v). In Part I, this profile was obtained from a WRF 3.3.1 real data simulation and was representative of the shear and instability conditions in which GCs were observed overnight in the 14–15 February 2010 cyclone (Figs. 5–7 of Part I). The idealized simulation in Part I with nighttime radiative forcing resulted in simulated GCs with w and q_i characteristics that compared favorably with observations from PLOWS (Tables 2–3 of Part I). Two layers of potential instability were present in the initial conditions, with θ_{ei} decreasing between 4.9 and 5.3 km and between 5.9 and 6.7 km at 0.98 and 0.40 K km^{-1}, respectively, corresponding to CAPE with respect to ice of 20.2 and 9.5 J kg^{-1}.

In Part II, initial conditions consisted of eight idealized stability profiles (Fig. 1), where the lower level of instability was removed by modifying θ so that θ_{ei} increased with height at a constant rate from its former maximum of 298.2 K at 4.9 km to 298.4 K at 5.9 km, the base of the upper layer of potential instability. The original θ_{ei} profile from Part I is shown in Fig. 1b in black, with modifications shown in blue. Above 5.9 km,

the stability profiles were in one of three categories: potentially unstable (profiles a–d, Fig. 1a), potentially neutral (profile e, Fig. 1a), and stable (profiles f–h, Fig. 1a).

In this paper, simulations were run for the same combinations of radiative forcing and instability as in Part II, but with six different shear profiles (Fig. 2). In these simulations, the wind profiles have been idealized so that there is no background wind below 4 km ($u = v = 0$ m s^{-1}). Above 4 km, profiles of u increase at rates of 0, 2, 4, 6, 8, and 10 m s^{-1} km^{-1} through 8.5 km, above which u remains constant through the model top of 15 km. The v component of the wind is 0 m s^{-1} in the initial conditions at all altitudes. The shear zone encompasses the region where GCs occurred in the model simulations of Part II. A summary of model initial conditions in terms of K–H instability is provided in Table 1, which shows the moist-ice bulk Richardson number Ri$_{Bmi}$ calculated over the 5.9–6.7-km layer for all combinations of stability (Fig. 1) and shear (Fig. 2) initial conditions in this paper. K–H instability is present in the initial conditions for all simulations with stability profile e (potentially neutral), all stable simulations with vertical wind shear ≥ 8 m s^{-1} km^{-1}, and all weakly stable (profile f) simulations with shear ≥ 6 m s^{-1} km^{-1}.

FIG. 6. Shear [m s⁻¹ km⁻¹], See Fig. 2 — Stability Profile, See Fig. 1

	Shear 0	2	4	6	8	10	Time
a	1.82	1.84	1.95	2.25	2.74	3.36	60
	2.03	2.01	1.91	1.99	2.03	2.11	120
	1.72	1.58	1.57	1.99	1.80	2.08	180
	2.19	2.04	1.95	2.25	2.80	3.54	MAX
b	1.74	1.74	1.81	2.08	2.45	2.97	60
	2.02	1.94	1.88	1.96	2.07	2.17	120
	1.73	1.60	1.59	1.65	1.85	2.02	180
	2.18	1.95	1.90	2.22	2.77	3.54	MAX
c	1.63	1.39	1.34	1.35	1.35	1.25	60
	2.04	1.84	1.81	1.93	2.15	2.35	120
	1.74	1.59	1.59	1.70	1.82	1.90	180
	2.13	1.88	1.88	2.19	2.83	3.60	MAX
d	1.25	0.64	0.57	0.53	0.49	0.45	60
	1.99	1.78	1.78	2.03	2.46	2.93	120
	1.76	1.61	1.60	1.68	1.74	1.75	180
	2.01	1.88	1.86	2.24	2.80	3.59	MAX
e	0.34	0.21	0.12	0.05	0.05	0.05	60
	1.84	1.95	2.05	2.34	2.81	3.41	120
	1.78	1.61	1.47	1.49	1.54	1.62	180
	1.98	1.97	2.06	2.44	3.00	3.78	MAX
f	0.18	0.05	0.05	0.05	0.05	0.05	60
	1.72	1.35	1.26	1.29	1.47	1.47	120
	1.79	1.40	1.27	1.36	1.62	1.87	180
	1.83	1.63	1.70	2.04	3.51	3.55	MAX
g	0.07	0.05	0.05	0.05	0.05	0.05	60
	1.50	1.21	1.15	1.01	1.00	1.00	120
	1.71	1.35	1.20	1.30	1.64	1.99	180
	1.71	1.48	1.60	1.90	2.49	3.30	MAX
h	0.05	0.05	0.05	0.05	0.05	0.05	60
	0.91	0.98	0.85	0.80	0.78	0.73	120
	1.56	1.26	1.09	1.24	1.65	2.09	180
	1.56	1.42	1.44	1.73	2.32	3.20	MAX

Nighttime Simulations 99th percentile of w [m s⁻¹]
- >3.00
- 2.00 – 3.00
- 1.00 – 1.99
- 0.25 – 0.99
- <0.25

FIG. 6. Summary of the 99th percentile of w in the 6–8-km layer (consistent with Figs. 3–5) as a function of stability, shear, and time for all simulations with nighttime radiative forcing. The stability categories a–h correspond to those shown in Fig. 1. The shear categories correspond to those shown in Fig. 2. Rectangular areas outlined in white (a–0, a–4, a–10, e–0, e–4, e–10, h–0, h–4, and h–10) indicate simulations for which CFTDs are shown in Fig. 3 and plan views are shown in Figs. 9 and 10.

FIG. 7. Shear [m s⁻¹ km⁻¹], See Fig. 2 — Stability Profile, See Fig. 1

	Shear 0	2	4	6	8	10	Time
a	1.47	1.55	1.72	2.12	2.66	3.35	60
	1.40	1.42	1.42	1.51	1.64	1.79	120
	1.12	1.11	1.16	1.37	1.61	1.67	180
	1.71	1.77	1.86	2.14	2.66	3.38	MAX
b	1.45	1.60	1.75	2.09	2.54	3.14	60
	1.43	1.39	1.38	1.52	1.68	1.84	120
	1.13	1.10	1.19	1.35	1.54	1.60	180
	1.52	1.63	1.73	2.09	2.63	3.39	MAX
c	1.41	1.49	1.53	1.60	1.92	2.15	60
	1.43	1.35	1.34	1.51	1.74	2.00	120
	1.14	1.09	1.19	1.36	1.44	1.44	180
	1.50	1.54	1.66	2.04	2.03	3.40	MAX
d	1.35	0.97	0.91	0.88	0.84	0.81	60
	1.44	1.26	1.32	1.59	2.04	2.43	120
	1.16	1.12	1.20	1.33	1.32	1.33	180
	1.47	1.43	1.59	2.03	2.66	3.39	MAX
e	0.73	0.43	0.34	0.29	0.24	0.20	60
	1.40	1.27	1.44	1.92	2.56	3.31	120
	1.18	1.10	1.14	1.19	1.24	1.28	180
	1.45	1.34	1.54	2.05	2.71	3.50	MAX
f	0.15	0.05	0.05	0.05	0.05	0.05	60
	1.52	0.93	0.99	1.22	1.57	1.97	120
	1.14	0.91	0.94	1.17	1.50	1.71	180
	1.52	1.13	1.27	1.81	2.55	3.35	MAX
g	0.05	0.05	0.05	0.05	0.05	0.05	60
	0.96	0.52	0.49	0.49	0.49	0.50	120
	0.93	0.78	0.81	1.25	1.81	2.33	180
	1.16	0.88	0.91	1.37	2.08	3.03	MAX
h	0.05	0.05	0.05	0.05	0.05	0.05	60
	0.43	0.38	0.35	0.35	0.35	0.35	120
	0.83	0.66	0.61	0.98	1.75	2.53	180
	1.09	0.71	0.65	0.99	1.75	2.78	MAX

Daytime Simulations 99th percentile of w [m s⁻¹]
- >3.00
- 2.00 – 3.00
- 1.00 – 1.99
- 0.25 – 0.99
- <0.25

FIG. 7. As in Fig. 6, but for simulations with daytime radiative forcing. Rectangular areas outlined in white indicate simulations for which CFTDs are shown in Fig. 4 and plan views are shown in Figs. 13 and 14.

b. Model settings

Aside from differences in the initial profiles of u and v, all model settings, including thermodynamics profiles and initial and lateral boundary conditions, for the simulations in this paper are the same as those for the simulations discussed in Part II. In summary, idealized WRF 3.3.1 simulations were integrated for 180 min on a $50.1 \times 50.1 \times 15$ km³ grid with horizontal grid spacing of 100 m, vertical level spacing of ~50 m near the GC level, and a dynamical time step of 0.5 s. Thompson microphysics and Rapid Radiative Transfer Model for Global Climate Models (RRTMG) radiation parameterizations were used, with a radiation time step of 30 s. The reader is referred to section 4a of Part I for detailed justification of the choice of microphysics and radiation schemes. The deep layer of nimbostratus below GCs was maintained as described in Part I using the large-eddy simulation of WRF (WRF-LES) module (Yamaguchi and Feingold 2012) using the prescribed ascent profile shown in Fig. 9 of Part I. All idealized simulations in this series were run on a doubly periodic (f plane) domain with f,

the Coriolis parameter equal to 10^{-4} s⁻¹, and radiative forcing (when included) consistent with southern Indiana on 15 February.

3. Results

a. Bulk properties of simulations

In total, 144 simulations were performed to assess the effects of instability, radiation, and shear on the generation and longevity of GCs. Statistical analyses of all simulations were carried out to compare the general evolution of w at the GC level (6–8 km) in a similar manner to that in Parts I and II. Contoured frequency by time diagrams (CFTDs; see Parts I and II) of w for selected combinations of stability, radiation, and shear are shown in Figs. 3–5. CFTDs of w show data every 5 min with a w bin width of 0.10 m s⁻¹.

Figure 3 shows CFTDs of w for simulations with nighttime radiative forcing (longwave only) under conditions of (from left to right) no shear, moderate shear (4 m s⁻¹ km⁻¹), and strong shear (10 m s⁻¹ km⁻¹) and stability conditions ranging from (from top to bottom) unstable (profile a, Fig. 1; $\Delta\theta_{ei}/\Delta z = -0.53$ K km⁻¹), neutral (profile e, Fig. 1; $\Delta\theta_{ei}/\Delta z = 0$ K km⁻¹), and stable (profile h, Fig. 1; $\Delta\theta_{ei}/\Delta z = +0.45$ K km⁻¹). Generating

Shear [m s⁻¹ km⁻¹], See Fig. 2

Stability Profile		0	2	4	6	8	10	Time
a		0.92	1.04	1.30	1.72	2.26	2.96	60
		0.72	0.72	0.73	0.92	1.24	1.57	120
		0.29	0.42	0.84	1.02	1.02	0.92	180
		1.40	1.42	1.48	1.77	2.27	3.02	MAX
b		0.90	1.17	1.27	1.62	2.07	2.62	60
		0.67	0.67	0.70	0.95	1.37	1.72	120
		0.33	0.48	0.81	0.98	0.95	0.90	180
		1.14	1.19	1.28	1.63	2.19	2.97	MAX
c		0.86	0.94	0.93	0.99	1.05	1.12	60
		0.59	0.61	0.80	1.08	1.61	2.11	120
		0.39	0.52	0.70	0.92	0.94	0.92	180
		0.91	0.94	1.05	1.48	2.14	2.98	MAX
d		0.51	0.47	0.47	0.45	0.43	0.42	60
		0.52	0.78	0.78	1.29	1.99	2.75	120
		0.49	0.68	0.68	0.89	0.99	1.04	180
		0.68	0.92	0.92	1.45	2.11	3.00	MAX
e		0.39	0.22	0.15	0.12	0.09	0.05	60
		0.49	0.50	0.55	0.54	0.55	0.61	120
		0.34	0.42	0.74	1.26	1.73	2.04	180
		0.60	0.52	0.87	1.51	2.24	3.11	MAX
f		0.05	0.05	0.05	0.05	0.05	0.05	60
		0.15	0.13	0.12	0.12	0.12	0.12	120
		0.22	0.28	0.26	0.23	0.20	0.32	180
		0.22	0.28	0.26	0.23	0.20	0.32	MAX
g		0.05	0.05	0.05	0.05	0.05	0.05	60
		0.14	0.11	0.11	0.11	0.11	0.11	120
		0.14	0.05	0.05	0.05	0.05	0.05	180
		0.14	0.12	0.11	0.11	0.11	0.11	MAX
h		0.05	0.05	0.05	0.05	0.05	0.05	60
		0.14	0.11	0.11	0.10	0.10	0.10	120
		0.13	0.05	0.05	0.05	0.05	0.05	180
		0.14	0.11	0.11	0.11	0.11	0.10	MAX

No Radiation Simulations 99th percentile of w [m s⁻¹]

- >3.00
- 2.00 – 3.00
- 1.00 – 1.99
- 0.25 – 0.99
- <0.25

FIG. 8. As in Fig. 6, but for simulations with no radiative forcing. Rectangular areas outlined in white indicate simulations for which CFTDs are shown in Fig. 5 and plan views are shown in Figs. 15 and 16.

cells develop in all simulations. GCs develop earlier with unstable conditions, with a broader range of w. GCs continue to develop through the end of the simulation. Under conditions without initial shear (Figs. 3a,d,g), as in Part II, as stability increases, the GCs develop later in time and have a narrower range of w. In all these three cases, a steady state develops. Updrafts have a slightly larger amplitude than downdrafts, with a mean difference between the magnitude of the 99th and 1st percentiles of w of 0.40 m s⁻¹ at t = 180 min.

For conditions of moderate shear (Figs. 3b,e,h), the range of w increases compared to the no-shear cases, shortly after the convection develops. These cases also attain a steady state. The difference between the magnitude of the 99th and 1st percentiles of w at the time of peak convection and at the time a steady state was achieved were larger compared to the no-shear cases. For the cases of moderate shear, the average range of w decreased by 0.77 m s⁻¹ between these two times for these three simulations. Unlike conditions of no shear, the w spectrum is generally symmetric, with little difference in magnitude between the 99th and 1st percentiles of w (0.1 m s⁻¹ average difference in magnitude at t = 180 min).

For conditions of strong shear (Figs. 3c,f,i) the simulation-long maximum 99th percentile of w during the

simulation was associated with the initial development of GCs. The role of K–H instability in enhancing the spread between the 1st and 99th percentiles of w during GC development in strong-shear simulations (see Table 1) will be discussed in section 3b(2). The 99th percentiles of w exceeded those of the corresponding GCs in the no-shear simulations by 62%, 91%, and 105% for the unstable, neutral, and stable stability profiles, respectively. At the end of the simulations the steady-state 99th percentiles of w for unstable and neutral conditions were within a 20% range of the no-shear simulations, suggesting no substantial difference. The stable, high-shear simulation had not yet reached a steady state at the end of the simulation.

Figure 4 shows the results for the same instability and shear profiles as in Fig. 3, but for daytime (longwave and shortwave) radiative forcing. In all cases, the maximum 99th percentile of w decreased regardless of shear magnitude or instability profile. The decrease in the no-shear simulations (Figs. 4a,d,g) from the nighttime simulations ranged from 22% to 30%. In the moderate-shear simulations (Figs. 4b,e,h), the decrease from the nighttime simulations was 5% for the unstable profile, 25% for the neutral profile, and 55% for the stable profile. For the high-shear simulations, the decrease from the nighttime simulations was less pronounced, ranging from 5% for the unstable profile to 16% for the stable profile. At 180 min, after a steady state was achieved, under no-shear conditions the decrease in the 99th percentile of w for daytime compared to nighttime ranged from 34% to 47% for the three different stability profiles in Figs. 3 and 4. For moderate shear, the decrease ranged from 22% to 44%, with the largest decrease for the stable profile. For the high-shear conditions, the decrease was ~20% for both the unstable and neutral profiles. The stable profile had not yet reached a steady state at the end of the simulation.

Figure 5 shows similar results to Fig. 4, but for no radiative forcing. GCs failed to develop for the stable profiles, regardless of shear (Figs. 5g,h,i). In the case of unstable initial conditions, the maximum 99th percentile of w increased with increasing shear, but the magnitude was reduced by 36%, 24%, and 15% for the no-shear, moderate-shear, and strong-shear simulations relative to the corresponding nighttime simulations (Figs. 5a,b,c). For the neutral simulations with no radiation, the maximum 99th percentile of w also increased with increasing shear. However, the magnitude again was reduced by 70%, 58%, and 18% for no shear, moderate shear, and strong shear relative to corresponding simulations with nighttime radiation. After 180 min, simulations with unstable and neutral initial profiles and no shear showed ongoing weakening of GCs, with a reduction in w

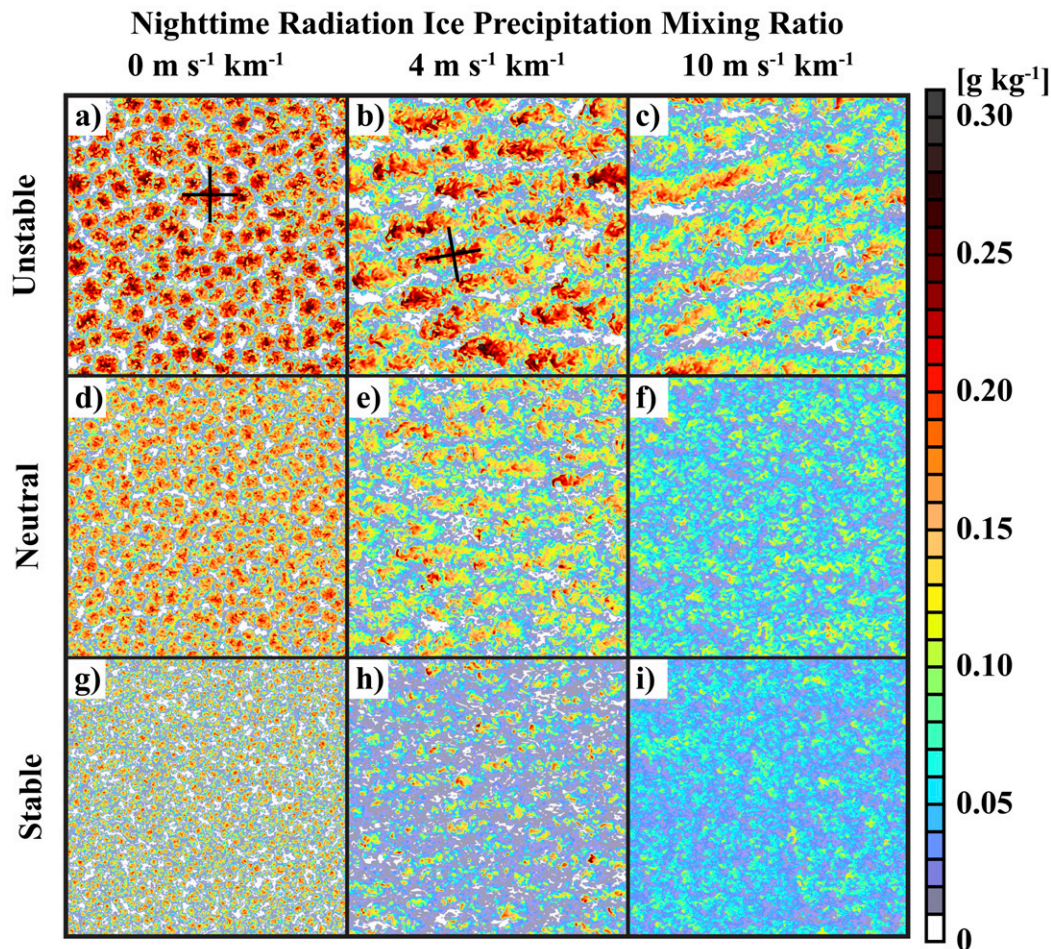## Nighttime Radiation Ice Precipitation Mixing Ratio

FIG. 9. Simulated ice precipitation mixing ratio at 7.5 km shown for the full horizontal extent of the model domain at $t = 180$ min in the nighttime radiation simulations. As in Fig. 3, rows correspond to stability profiles and columns correspond to u shear. The black lines in (a) and (b) indicate the locations of the cross sections shown in Figs. 11 and 12, respectively.

amplitude of 81%–83% compared to the corresponding nighttime simulations. The initially unstable and neutral simulations with moderate shear came to a near-steady state. However, the 99th percentile of w was reduced by 24% for the unstable simulation and 58% for the neutral simulation compared to the nighttime simulation. The strong-shear, unstable simulation with no radiation generated large-amplitude (99th percentile of $w = 3.59 \, \mathrm{m \, s^{-1}}$) GCs ~60 min into the simulation. Following the peak 99th percentile of w, a substantial downward trend in w magnitude continued through the end of the simulation, with a reduction in the 99th percentile of w to $0.92 \, \mathrm{m \, s^{-1}}$ at $t = 180$ min (a 56% decrease relative to the corresponding nighttime simulation). The strong-shear, neutral simulation with no radiation did not attain a steady state by the end of the simulation; however, a downward trend in w was present following the peak w at ~150 min.

Complete statistics for all 144 simulations appear in Figs. 6, 7, and 8 for nighttime, daytime, and no radiative forcing, respectively. Specifically, in Figs. 6–8, the values of the 99th percentile of w are shown for $t = 60, 120,$ and 180 min, as well as the simulation maximum 99th percentile of w. In the following discussion, the vigor of GCs (consisting of precipitation maxima, as required by the AMS definition) or lack thereof is characterized by the 99th percentile of w as follows: none ($w < 0.25 \, \mathrm{m \, s^{-1}}$), weak ($0.25 \leq w \leq 0.99 \, \mathrm{m \, s^{-1}}$), moderate ($1.00 \leq w \leq 1.99 \, \mathrm{m \, s^{-1}}$), strong ($2.00 \leq w \leq 2.99 \, \mathrm{m \, s^{-1}}$), or substantial ($w \geq 3.00 \, \mathrm{m \, s^{-1}}$). It is important to note that q_i maxima generated by the release of shear instability (i.e., K–H waves) fits the AMS definition of GCs as long as a precipitation fall streak is produced.

GCs developed and persisted in all simulations with nighttime radiative forcing, regardless of initial stability or shear (Fig. 6). Substantial GCs were present in all
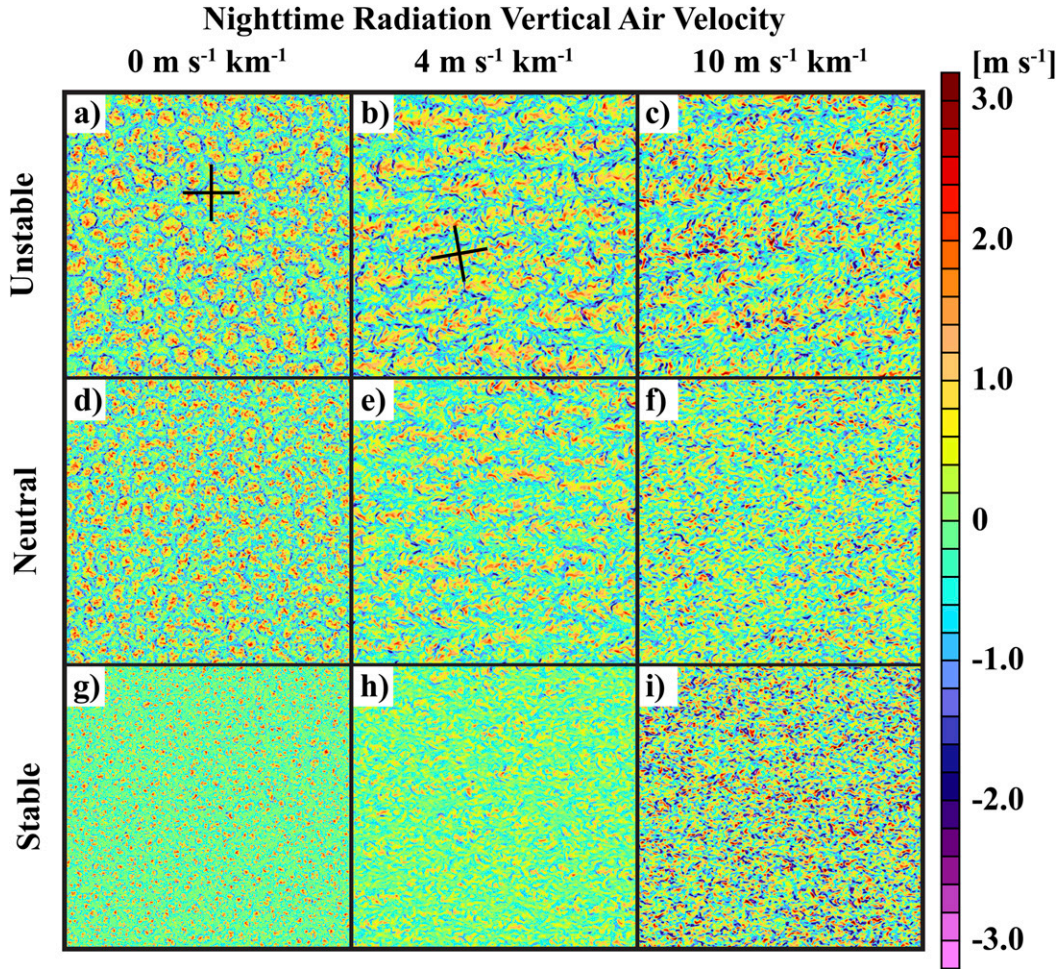
Nighttime Radiation Vertical Air Velocity

FIG. 10. As in Fig. 9, but for *w*.

nighttime simulations with shear of $10\,m\,s^{-1}\,km^{-1}$ and in the initially neutral or weakly stable simulations with shear of $8\,m\,s^{-1}\,km^{-1}$. Moderate or strong GCs developed prior to $t = 60\,min$ for all nighttime simulations with stability profiles a–c (see Fig. 1). For the weakly unstable initial conditions (profile d), weak GCs developed by $t = 60\,min$ and evolved into moderate to strong GCs for all but the strongest shear profile, in which substantial GCs developed. For the most stable simulations (profiles e–h), GCs did not develop prior to 60 min, although they all developed moderate to substantial GCs after 60 min (profiles f and g), or 120 min (profile h). Even in the most stable conditions, substantial GCs developed by the end of the simulations with the strongest shear.

Moderate to strong GCs also developed early in the daytime simulations with stability profiles a–c (Fig. 7); substantial GCs were present early in the simulations with the strongest shear profile for these same stability

profiles. For the most stable profiles (g and h), with shear up to $4\,m\,s^{-1}\,km^{-1}$, only weak GCs developed by the end of the simulations, with no GCs present at 60 min. For stronger shear between 6 and $8\,m\,s^{-1}\,km^{-1}$, moderate to strong GCs developed by the end of the simulations with stability profiles g and h, and, for the strongest shear $(10\,m\,s^{-1}\,km^{-1})$, strong to substantial GCs developed by the end of the simulations. In all these simulations with instability profiles g and h, GCs did not develop prior to 60 min into the simulation. In the intermediate profiles (d–f), weak to moderate GCs progressively took longer to develop as the initial stability was increased. The strongest GCs in these categories at the end of these simulations (of up to substantial strength) were associated with the strongest shear profiles.

The evolution of GCs was substantially different in simulations with no radiative forcing (Fig. 8). GCs did not develop regardless of shear in simulations with
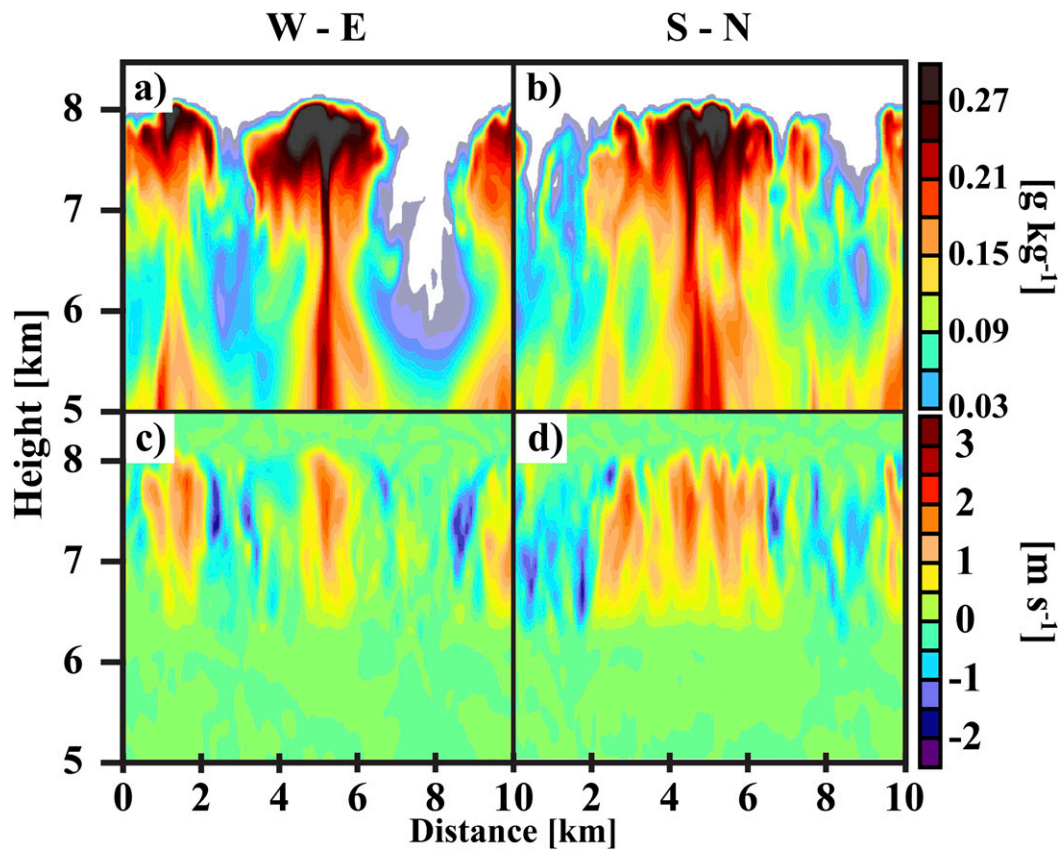
FIG. 11. Perpendicular cross sections of (a),(b) ice precipitation mixing ratio and (c),(d) vertical air velocity at $t =$ 180 min in the most unstable, no-shear, nighttime radiation simulation, wherein GCs organized into closed-cell convection. The location of the cross sections is indicated by black lines in Figs. 9a and 10a.

stability profiles g and h, and only marginally weak GCs developed in a few simulations with stability profile f. In nearly all simulations that did develop GCs, the strongest convection occurred early and diminished in intensity through the remainder of the simulations. At 180 min, only weak GCs were present in stability profiles c, d, and e with shear profiles of $4 \, \mathrm{m \, s^{-1} \, km^{-1}}$ or less. The only category with strong GCs at 180 min was stability profile e with the strongest shear profile ($10 \, \mathrm{m \, s^{-1} \, km^{-1}}$). The effect of shear in the absence of radiation in generating GCs was most pronounced when the initial atmospheric profiles were unstable or neutral.

b. Organization and structure of convection

Another potential effect of shear, in addition to affecting the amplitude of GC circulations, is to impact the manner in which GCs are organized. The structures produced in all 144 simulations progressed systematically for conditions of stability, shear, and radiative forcing. These changes will be summarized below using

the same subset of simulations as shown in Figs. 3–5 (see also highlighted boxes in Figs. 6–8).

1) WEAK TO MODERATE SHEAR

Figures 9 and 10 show the organization of the ice precipitation mixing ratio field q_i ($\mathrm{g \, kg^{-1}}$; sum of cloud-ice and snow mixing ratios; see Parts I and II) and w, respectively, at 7.5 km and 180 min into the simulations with nighttime radiative forcing. In the cases of no shear, visual inspection indicates that the GCs were organized into closed convective cells (Figs. 9a,d,g, 10a,d,g). This closed convective cell structure is further highlighted in two perpendicular cross sections through a representative GC (shown in Fig. 11) for the most unstable, no-shear, nighttime radiation simulation.

As stability increased, the cells had progressively weaker w (the 99th percentiles of w in the 6–8-km layer at $t = 180$ min were 1.72 and 1.57 $\mathrm{m \, s^{-1}}$ for the most unstable and most stable profiles, respectively), smaller horizontal dimensions, and lower q_i (typical maxima > 0.25 and $\sim 0.20 \, \mathrm{g \, kg^{-1}}$ for the most unstable and most stable
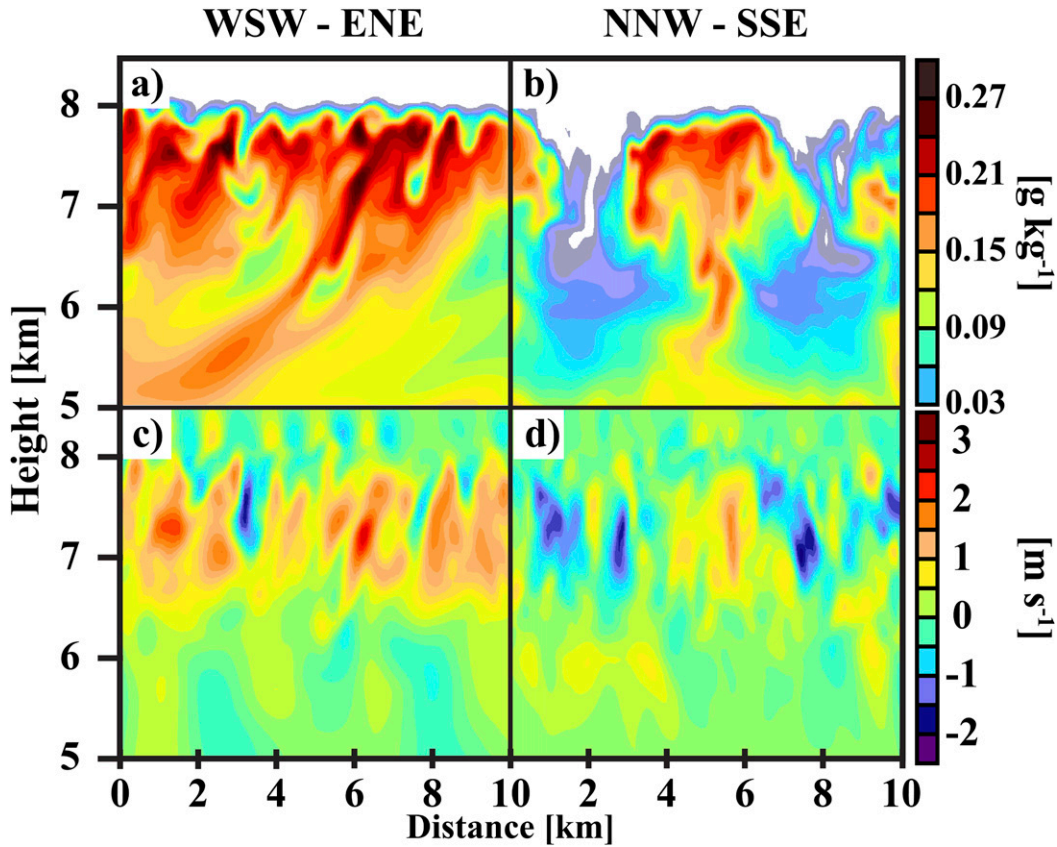
FIG. 12. As in Fig. 11, but for the most unstable, moderate-shear (4 m s^{-1} km^{-1}) nighttime radiation simulation, wherein GCs organized into roll-like convection. The location of cross sections is indicated by the black lines in Figs. 9b and 10b.

profiles, respectively). Additionally, the horizontal dimension of GCs was smaller with daytime relative to nighttime radiative forcing. This is particularly evident in the no-shear, initially unstable simulations (Figs. 9a, 13a) and is consistent with Shao and Randall (1996), who concluded that stronger cloud-top cooling is associated with wider cells within stratocumulus. The organization of the GCs changed to an appearance more like cloud streets for the unstable and neutral, moderate-shear simulations (Figs. 9b,e, 10b,e). As stability was increased further (Figs. 9h, 10h) distinct circulations became less coherent. When present, the cloud-street structures were oriented west-southwest–east-northeast. The mean wind direction in these simulations slowly shifted from west to west-southwest during the course of the simulations. The orientation of these streets of GCs is consistent with the wind direction as expected by theory for horizontal convective rolls (Asai 1970a,b). As one would expect from the plan views showing cloud-street structures (Figs. 9b,e, 10b,e), the structure in cross sections through these GCs is highly dependent on the

orientation of the cross section, as illustrated in Fig. 12. The cross section along the cloud street is characterized primarily by updrafts located from 6.5 to 8.0 km collocated with $q_i = 0.15$–0.30 g kg^{-1} and multiple fall streaks (Figs. 12a,c). The cross-section perpendicular to this consists of a broad updraft collocated with q_i of a similarly high magnitude and a single precipitation fall streak, surrounded by broad downdrafts and $q_i < 0.03$ g kg^{-1} (Figs. 12b,d). As expected, the fall streaks are sheared.

For the daytime simulations, the organization of the precipitation was similar to the nighttime simulations, except that the vertical velocities were weaker and the ice precipitation mixing ratio values were smaller (Figs. 13, 14). Consistent with results of Parts I and II, there was a somewhat greater spacing between GCs relative to corresponding simulations with nighttime radiative forcing, at least in the no-shear and moderate-shear simulations. GC spacing at $t = 180$ min, as indicated by Fourier analysis of the w field at 7.5 km, shown in Figs. 10 and 14, was 4.2 and 2.4 km for the nighttime and daytime simulations with stability

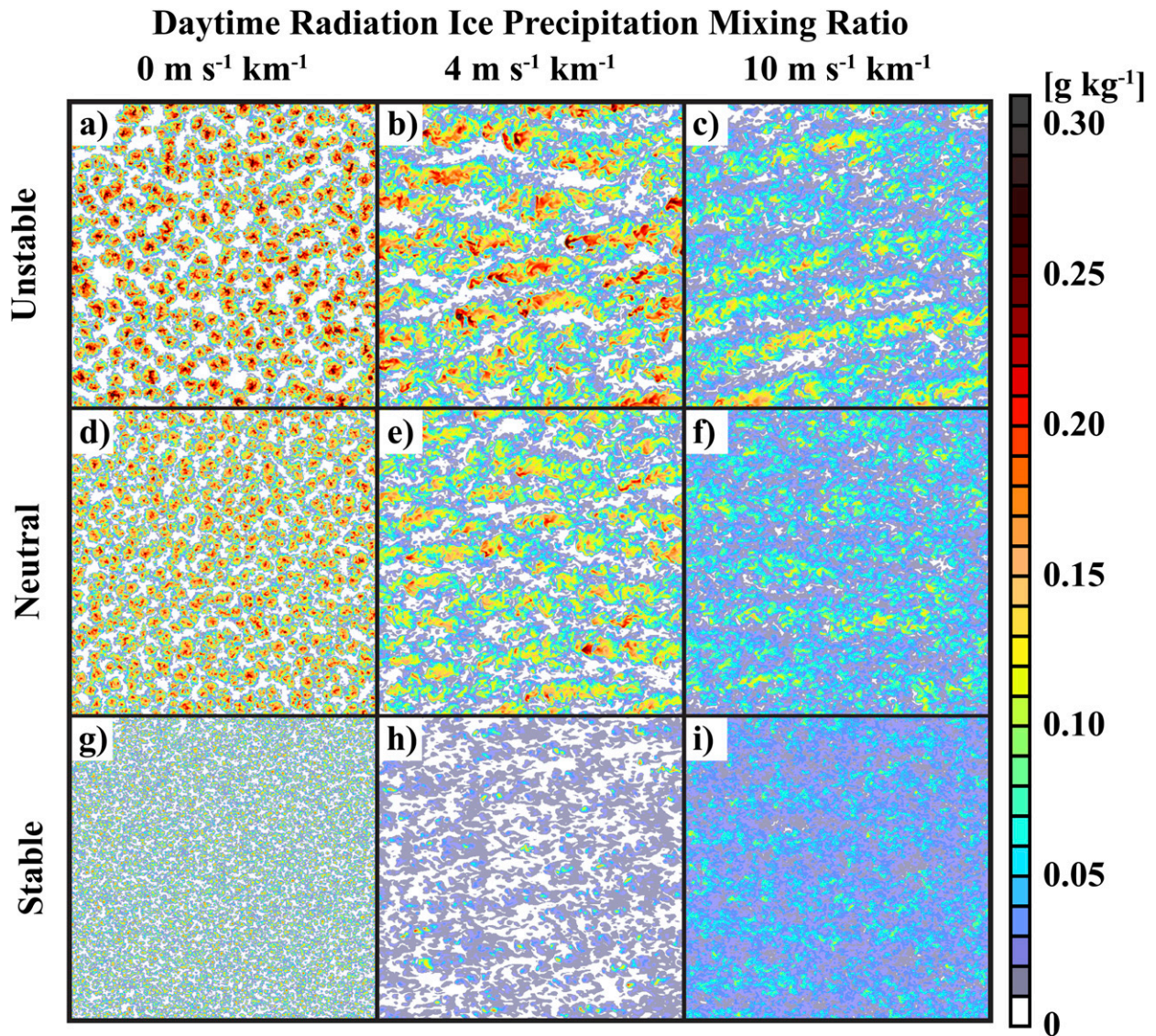## Daytime Radiation Ice Precipitation Mixing Ratio

FIG. 13. As in Fig. 9, but for the daytime radiation simulations.

profile a and no shear (see Figs. 10a, 14a) and 6.3 and 5.6 km for nighttime and daytime simulations with stability profile a and moderate shear (4 m s^{-1} km^{-1}; see Figs. 10b, 14b). At the same simulation time, GC spacing was 4.2 and 2.3 km for the nighttime and daytime simulations with stability profile e and no shear (see Figs. 10d, 14d). GC spacing was 4.5 km in the moderate-shear, stability profile e simulations with both nighttime and daytime radiative forcing (see Figs. 10e, 14e).

No GCs developed in the initially stable simulations with no radiative forcing (Figs. 15g–i, 16g–i). In the unstable and neutral simulations with no shear, the GCs were exceptionally weak, with no clear organization.

In the moderate-shear simulations, linear organization of the weak cells was apparent.

2) STRONG SHEAR

For the nighttime, high-shear simulations, cloud-street structures were apparent only in the unstable simulation (Figs. 9c, 10c). In these simulations, the decrease in θ_{ei} with height causes Ri_{Bmi} to be negative in the initial conditions, which favors convection dominated by buoyancy rather than K–H instability. The initially neutral and stable high-shear simulations with nighttime radiative forcing produced somewhat incoherent patterns, although some indication of linear structure can be discerned from a careful look at

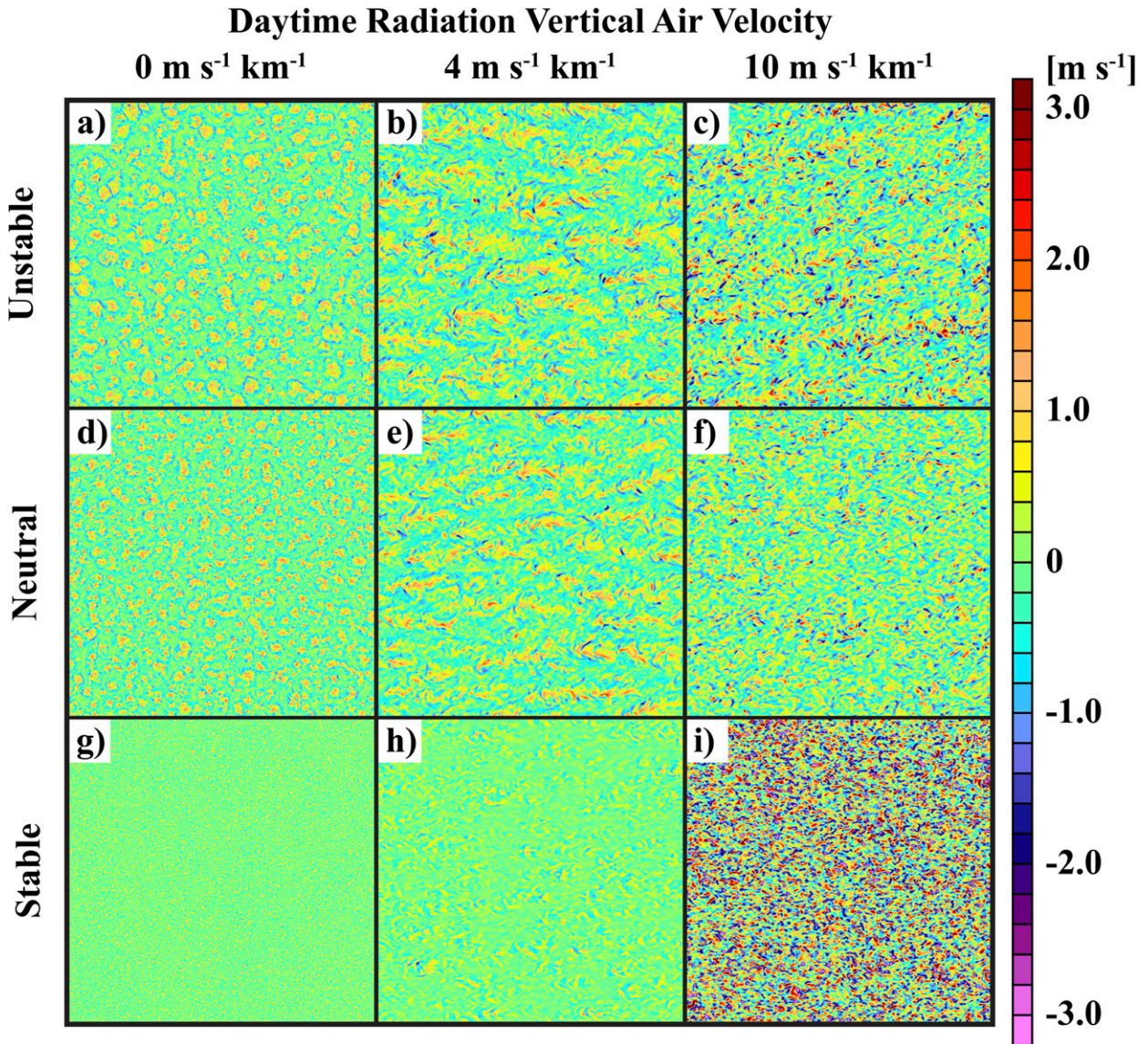## Daytime Radiation Vertical Air Velocity

FIG. 14. As in Fig. 10, but for the daytime radiation simulations.

Figs. 9f,i and 10f,i. The general decrease in cloud-street coherence simulations with increased initial stability is also seen in the daytime radiation simulations.

Some clarity can be achieved in regard to these less coherent structures under high shear when considering K–H instability. Figure 17 shows the evolution of domain-averaged profiles of θ_{ei}, u, and v from 5 to 8.5 km from t = 90 to 135 min for the initially neutral, strong-shear, nighttime radiation simulation (Figs. 3f, 9f, 10f). At t = 90 min, GCs had not yet developed; however, the θ_{ei} profile clearly shows that some potential instability had developed, with θ_{ei} decreasing from 298.3 to 298.0 K between 5.9 and 7.2 km [a rate close to that initially present in simulations with stability profile c (Fig. 1) but

over a deeper layer]. Above this layer, θ_{ei} increased with height in the presence of strong shear. At t = 105 min, convection developed both within the layer of potential instability and above, with the latter taking the form of K–H waves (Fig. 18). Based on the presence of K–H waves in the ~(7.3–7.8)-km layer seen in Fig. 18, Ri_{Bmi} was calculated over that layer at t = 90, 105, 120, and 135 min. Over this time period, Ri_{Bmi} continually decreased (0.07, 0.06, 0.03, and 0 at t = 90, 105, 120, and 135 min) as a result of cooling at the top of this layer and an overall decrease in shear due to mixing. By t = 150 min, Ri_{Bmi} had decreased further to −0.2. In summary, this time period consisted of a rapid increase in spread of w (Fig. 3f) consistent with release of
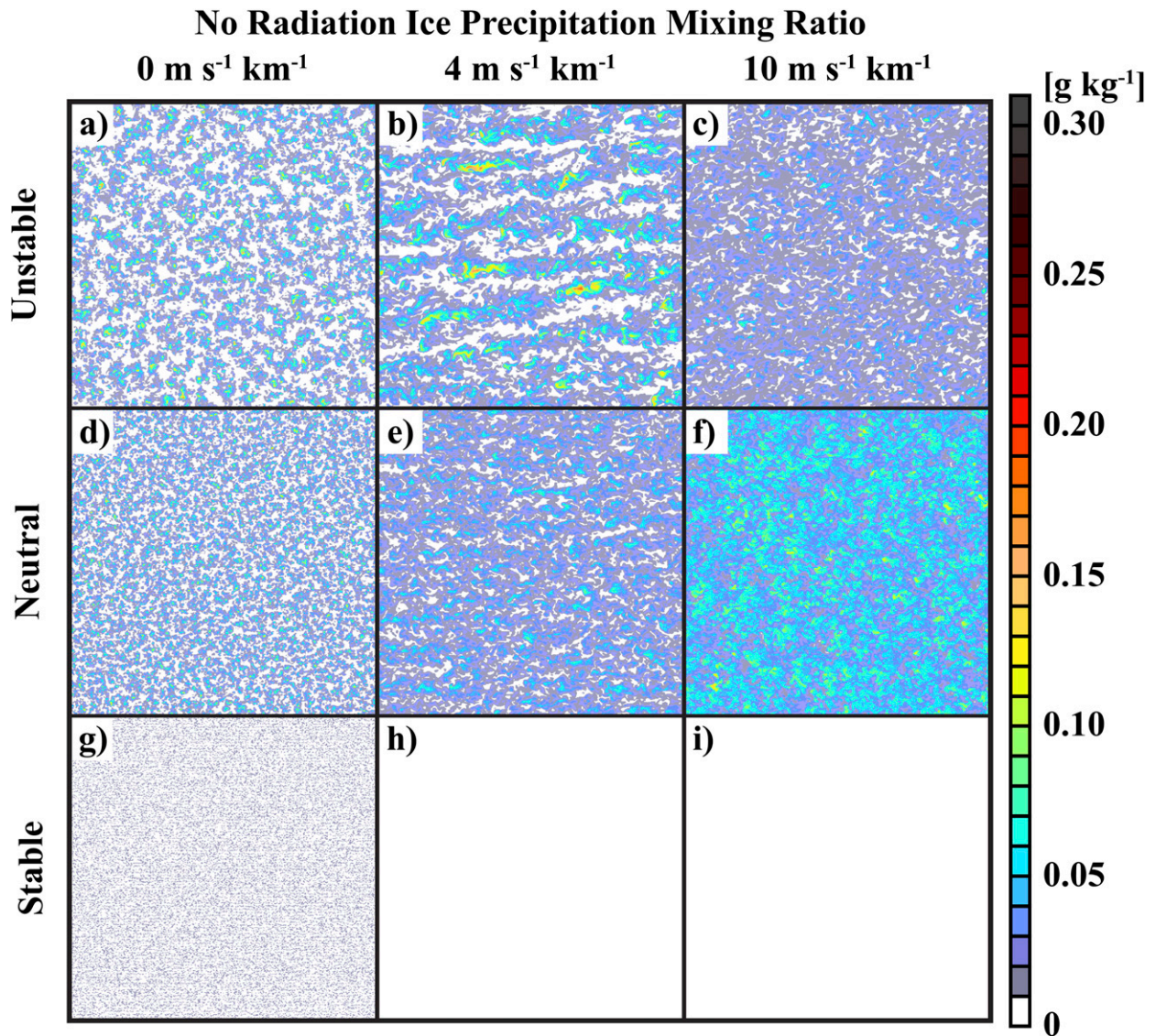
FIG. 15. As in Fig. 9, but for the no-radiation simulations.

shearing instability as radiation destabilized the atmosphere, followed by equilibration to a weaker shear profile.

4. Discussion

Generating cells are a common feature observed at the top of the otherwise stratiform comma-head regions of winter cyclones (Carbone and Bohne 1975; Syrett et al. 1995; Evans et al. 2005; Cunningham and Yuter 2014; Kumjian et al. 2014; Rauber 2014a,b; Rosenow et al. 2014; Plummer et al. 2014, 2015). The cloud-top region of cyclones is often characterized by some amount of vertical wind shear because of its proximity to the tropopause (Luce et al. 2002; Pavelin et al. 2002). In Parts I and II, the relationship between cloud-top GCs,

radiative forcing, and instability was examined using a single shear profile characteristic of the 14–15 February 2010 southern Indiana winter cyclone observed during the PLOWS campaign. In those papers, we provided a quantitative analysis of the radiative cooling and heating rates, latent heating, updraft and downdraft magnitude and structure, and ice precipitation mixing ratio in cloud-top GCs. In this paper, we have expanded the suite of idealized simulations in Part II to examine the effects of vertical wind shear.

Vertical wind shear affected the time required for destabilization and subsequent GC formation, as well as GC organization and intensity. Regarding organization, the simulations showed that, in the absence of shear, cloud-top convection, driven by cloud-top radiative
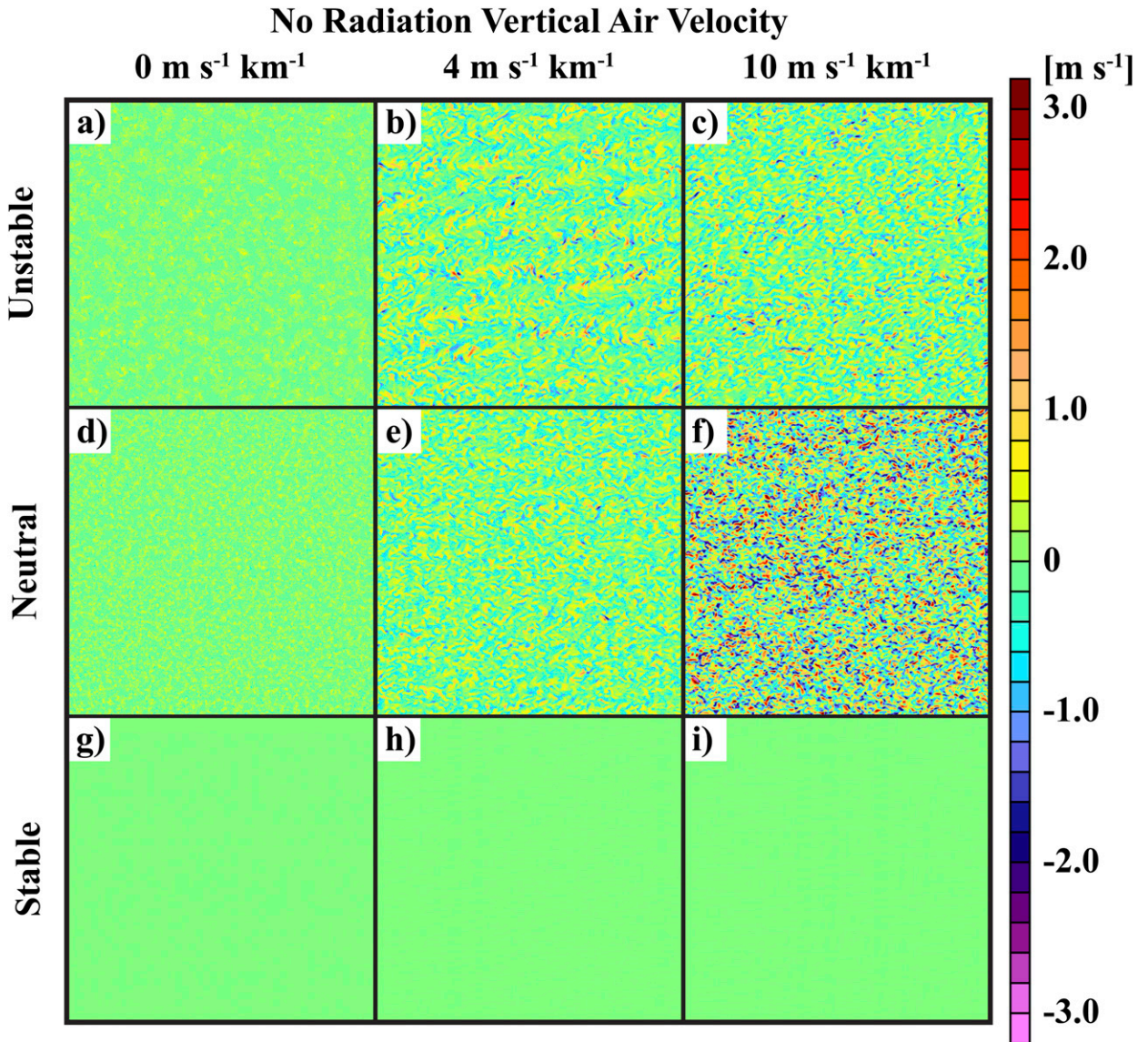
No Radiation Vertical Air Velocity

FIG. 16. As in Fig. 10, but for the no-radiation simulations.

cooling, organized as closed cell convection. This type of circulation consists of broad updrafts surrounded by narrow downdrafts (e.g., Fig. 10a). Similar circulations have been observed in stratocumulus clouds [see reviews by Atkinson and Zhang (1996) and Wood (2012)]. As in the case of their boundary layer counterparts, GCs organized into closed-cell convection in the absence of shear (Miura 1986; Shao and Randall 1996), suggesting that the radiative forcing for closed-cell convection for cloud-top generating cells has similarities to stratocumulus (Nicholls 1989; Shao and Randall 1996). The effect of shear was to reorganize the GCs into linear roll-like structures (e.g., Asai 1970a,b; Holroyd 1971; LeMone 1973; Young et al. 2002). However, these

circulations differed from boundary layer rolls in that they are not forced by heating from below, but rather by cooling from aloft. The overall organization of GCs is also well predicted by Ri_{Bmi}, as shown in Table 2. As in Kuo (1963), cloud-street structures were favored for $0 > Ri_{Bmi} > -2$. Simulations with $Ri_{Bmi} < -2$ produced GCs that organized as closed-cell convection.

The complete suite of simulations shows that the primary forcing for cloud-top GCs is radiation. Table 2 shows statistics for updraft intensity independent of shear for the nighttime, daytime, and no-radiation simulations. The summary statistics are for the 99th-percentile value of w during each simulation. The statistics show the mean, median, and highest value of the 99th-percentile value of
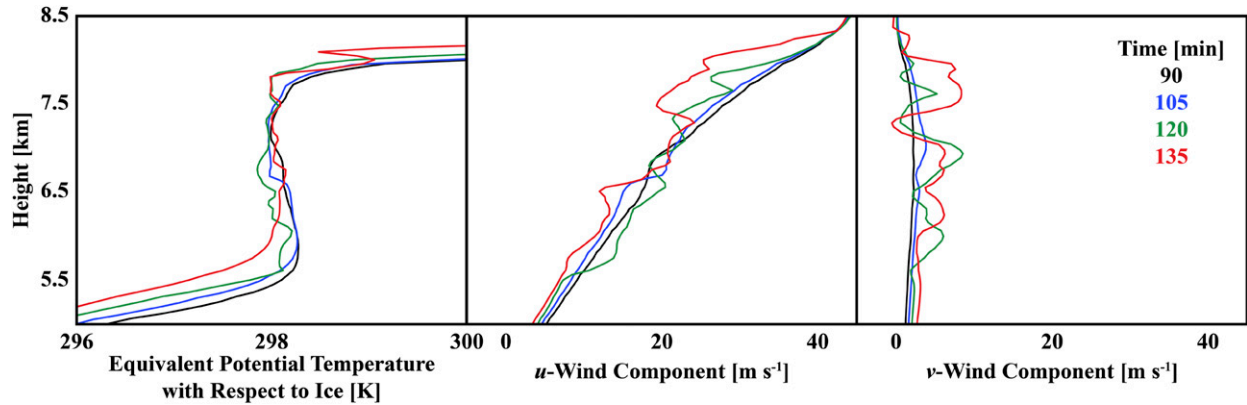
FIG. 17. Domain-averaged profiles of θ_{ei}, u, and v at $t = 90$, 105, 120, and 135 min (black, blue, green, and red lines) in the initially neutral, strong-shear ($10 \text{ m s}^{-1} \text{ km}^{-1}$), nighttime radiation simulation.

w achieved anytime during the simulation, and the mean, median, and maximum value of w 180 min into the simulation, provided the simulation had achieved a steady state (6 of 144 simulations were not included in the summary statistics because w was still changing rapidly at the time the simulation was terminated). The data in Table 2 show the importance of radiative forcing to the intensity of the updrafts in the GCs. Note that typical steady-state values of the 99th percentile of w with radiative forcing lie between 1.19 and 2.08 m s^{-1}, values
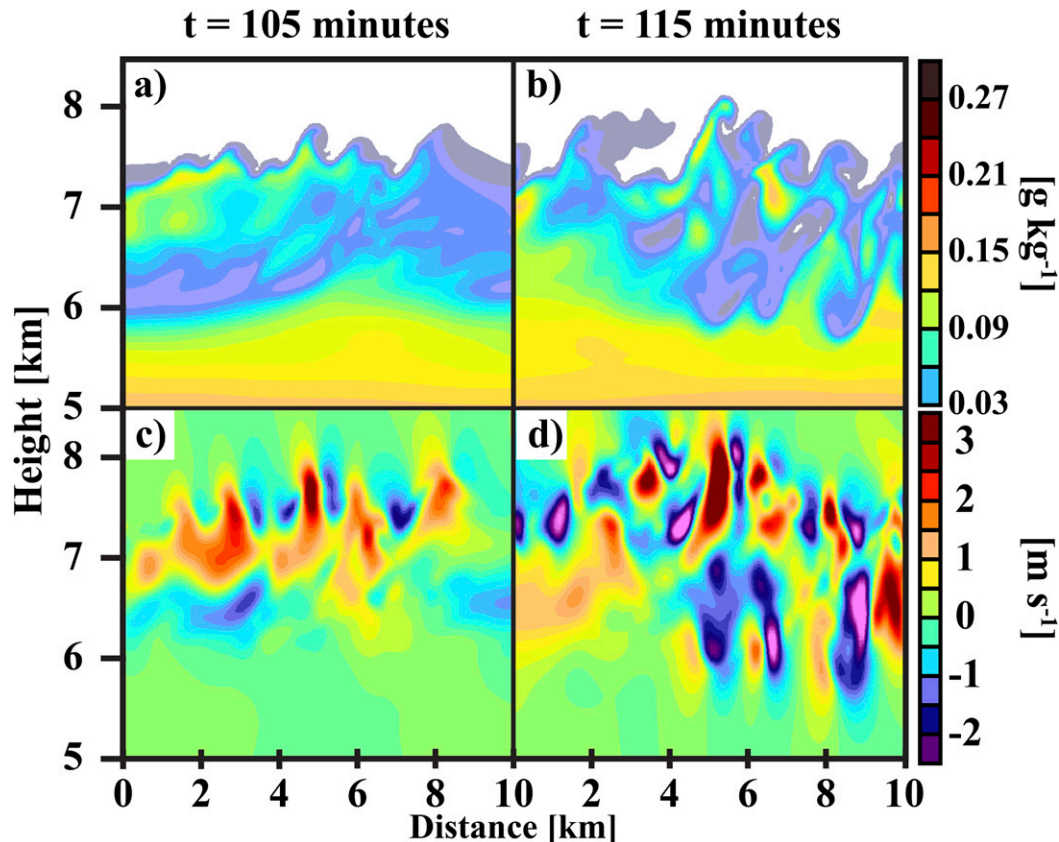

FIG. 18. West-to-east cross sections of (a),(b) ice precipitation mixing ratio and (c),(d) vertical air velocity at $t = $ (left) 105 and (right) 115 min in the initially neutral, strong ($10 \text{ m s}^{-1} \text{ km}^{-1}$) shear, nighttime radiation simulation. K–H waves were apparent at these times.

TABLE 2. Summary statistics for simulation-long maximum and steady-state 99th percentile of w (at $t = 180$ min). Six simulations are excluded from these statistics because of failure to achieve a steady state by the end of those simulations (see text).

	Maximum 99th percentile of w	99th percentile of w at 180 min
Nighttime		
Mean	2.33	1.63
Median	2.10	1.64
Maximum	3.78	2.08
Daytime		
Mean	1.95	1.22
Median	1.75	1.19
Maximum	3.50	1.81
No radiation		
Mean	1.09	0.49
Median	0.92	0.42
Maximum	3.11	1.04

consistent with the data presented in Part I. Shear acted to organize the clouds differently and, in the case of strong shear, increased the range of w due to the short-lived presence of K–H waves near cloud top. The impact of increasing shear can be seen graphically by examining the evolution of the 99th percentile of w, averaged over the full domain, at 180 min into each simulation for each stability profile for the nighttime, daytime, and no-radiation classes of simulations (Fig. 19). In the simulations where either nighttime or daytime radiative forcing is present, the strongest updrafts for any stability profile occur either with no shear or strong shear ($10 \, m \, s^{-1} \, km^{-1}$). A distinct w minimum occurred in all simulations with radiative forcing with shear = $4 \, m \, s^{-1} \, km^{-1}$. This behavior can be related to the transition between circulations dominated by closed cell convection (no shear) and circulations dominated by roll-like convection (strong shear).

This is consistent with organization of convection in stratocumulus rooted in the planetary boundary layer, where cellular, nonlinear convection is typically observed when shear is $\leq 2 \, m \, s^{-1} \, km^{-1}$ (Shao and Randall 1996). Similar behavior was not observed in the no-radiation simulations where the only mechanisms available to form and maintain GCs were the initial instability and shear. GCs failed to develop in the stable simulations in the absence of radiative forcing.

A caveat worth noting is that these simulations did not account for changes in the vertical wind shear profile due to synoptic-scale processes. Therefore, it is possible that, under the right conditions, K–H waves could persist longer than they did in the simulations analyzed in this paper. Specifically, this could be favored in environments where differential thermal advection (warm air advection near cloud top, with cold air advection below) is sufficient to offset the destabilizing influence of longwave radiative forcing and allow for persistence of positive $Ri_{Bmi} < 0.25$. It is interesting to note that an initially stable cloud layer with nonzero vertical wind shear that is undergoing destabilization (e.g., driven by radiative forcing) will be characterized by K–H instability for an undefined period of time prior to becoming potentially unstable.

As discussed in the introduction to Part I, numerous studies over the past 65 yr have reported the existence of generating cells at the top of stratiform cloud systems associated with the comma head of extratropical cyclones. This three-part series of papers showed that the primary forcing for these generating cells is radiative cooling. The intensity and organization of the cells are modulated by the stability characteristics of the environment in which they form, whether or not shortwave radiative forcing is present to offset cloud-top destabilization, and the vertical shear profile across the
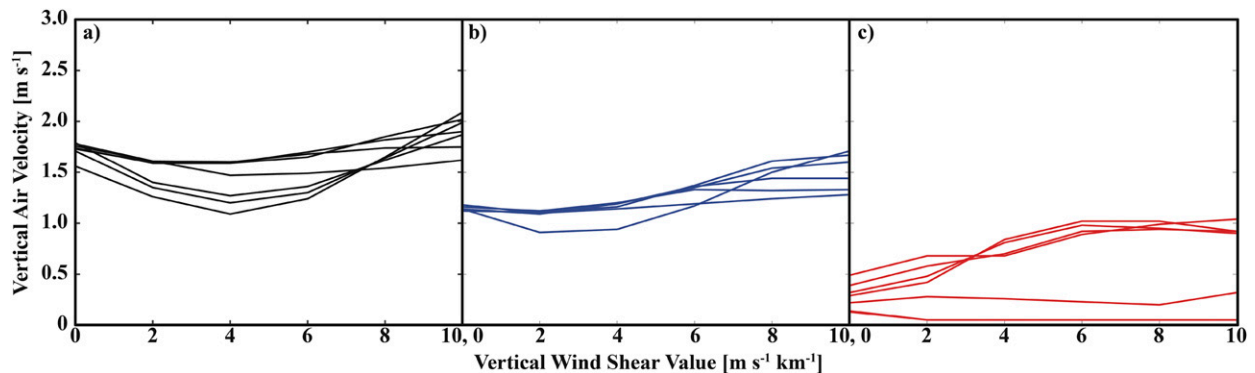

FIG. 19. Variation of the 99th percentile of w as a function of shear at 180 min into each simulation for each stability profile for the (a) nighttime, (b) daytime, and (c) no-radiation classes of simulations. Six simulations are excluded from these statistics as a result of failure to achieve a steady state by the end of those simulations (see text).

altitudes at which the generating cells occur. As discussed by Plummer et al. (2014, 2015), generating cells are responsible for the initial production of ice crystals that eventually lead to snowfall at the ground. Paired with the fact that GCs were commonly observed in WCR flight legs in stratiform regions during PLOWS, the development of GCs in all simulations with radiative forcing performed for Parts I, II, and III provides strong evidence for the observed ubiquity of GCs at cloud top in the comma head of extratropical cyclones and their importance to the structure and complexity of precipitation processes in winter storms.

5. Summary

This paper is the third in a series examining the forcing for cloud-top generating cells atop stratiform clouds within the comma head of winter cyclones. This paper specifically focuses on the role of shear in both the organization and intensity of updrafts associated with generating cells under conditions of nighttime, daytime, and no radiative forcing. The key findings are as follows:

- The primary role of shear is to modulate the organization of cloud-top convection. In the case of no shear, when radiative forcing was present, cloud-top convection organized as closed convective cells, similar in structure to those observed in stratocumulus forced by cloud-top cooling in the absence of shear. In the case where shear and radiative forcing were present, generating cells organized in linear streets parallel to the shear vector, similar to roll-like convection.
- No GCs developed in the initially stable simulations with no radiative forcing. In the unstable and neutral simulations with no shear and no radiative forcing, the GCs were exceptionally weak, with no clear organization. In the moderate-shear simulations ($\Delta u/\Delta z \sim 4\,\mathrm{m\,s^{-1}\,km^{-1}}$) linear organization of the weak cells was apparent. Linear organization was less apparent in simulations with high shear.
- The intensity of the updrafts associated with generating cells was primarily related to the mode of radiative forcing (nighttime, daytime, or no radiation). However, the intensity was modulated by shear with the more intense generating cells either associated with no shear (closed convective cells) or strong shear (roll-like linear streets). The strongest updrafts were in simulations with the strongest shear during a short-lived period of K–H waves concurrent with the development of generating cells.
- In all the simulations, the range of updrafts observed within generating cells under conditions of daytime or

nighttime radiative forcing was typically $\sim$1–2 m s^{-1}, with maximum values $< 4\,\mathrm{m\,s^{-1}}$.
- The horizontal structure of simulated generating cells is remarkably similar to convective structures observed in the planetary boundary layer. Moreover, the shear magnitude required for generating cells to transition from closed cells to roll-like convection is consistent with their boundary layer counterparts. These results suggest that efforts should be made to observe the finescale horizontal structure and temporal evolution of upper-tropospheric convection in future field campaigns.

REFERENCES

American Meteorological Society, 2016: Generating cell. Glossary of Meteorology. [Available online at http://glossary.ametsoc.org/wiki/Generating_cell.]

Asai, T., 1970a: Stability of a plane parallel flow with variable wind shear and unstable stratification. *J. Meteor. Soc. Japan*, **48**, 129–139, doi:10.2151/jmsj1965.48.2_129.

——, 1970b: Three-dimensional features of thermal convection in a plane Couette flow. *J. Meteor. Soc. Japan*, **48**, 18–29, doi:10.2151/jmsj1965.48.1_18.

Atkinson, B. W., and J. W. Zhang, 1996: Mesoscale shallow convection in the atmosphere. *Rev. Geophys.*, **34**, 403–431, doi:10.1029/96RG02623.

Carbone, R. E., and A. R. Bohne, 1975: Cellular snow generation—A Doppler radar study. *J. Atmos. Sci.*, **32**, 1384–1394, doi:10.1175/1520-0469(1975)032<1384:CSGDRS>2.0.CO;2.

Case, K. M., 1960: Stability of inviscid plane Couette flow. *Phys. Fluids*, **3**, 143–148, doi:10.1063/1.1706010.

Cunningham, J. G., and S. E. Yuter, 2014: Instability characteristics of radar-derived mesoscale organization modes within cool-season precipitation near Portland, Oregon. *Mon. Wea. Rev.*, **142**, 1738–1757, doi:10.1175/MWR-D-13-00133.1.

Douglas, R. H., K. L. S. Gunn, and J. S. Marshall, 1957: Pattern in the vertical of snow generation. *J. Meteor.*, **14**, 95–114, doi:10.1175/1520-0469(1957)014<0095:PITVOS>2.0.CO;2.

Dyson, F. J., 1960: Stability of an idealized atmosphere. II. Zeros of the confluent hypergeometric function. *Phys. Fluids*, **3**, 155–157, doi:10.1063/1.1706012.

Evans, A. G., J. D. Locatelli, M. T. Stoelinga, and P. V. Hobbs, 2005: The IMPROVE-1 storm of 1–2 February 2001. Part II: Cloud structures and the growth of precipitation. *J. Atmos. Sci.*, **62**, 3456–3473, doi:10.1175/JAS3547.1.

Geerts, B., and Q. Miao, 2010: Vertically pointing airborne Doppler radar observations of Kelvin–Helmholtz billows. *Mon. Wea. Rev.*, **138**, 982–986, doi:10.1175/2009MWR3212.1.

Holroyd, E. W., 1971: Lake-effect cloud bands as seen from weather satellites. *J. Atmos. Sci.*, **28**, 1165–1170, doi:10.1175/1520-0469(1971)028<1165:LECBAS>2.0.CO;2.

Houser, J. L., and H. B. Bluestein, 2011: Polarimetric Doppler radar observations of Kelvin–Helmholtz waves in a winter storm. *J. Atmos. Sci.*, **68**, 1676–1702, doi:10.1175/2011JAS3566.1.

Keeler, J. M., B. F. Jewett, R. M. Rauber, G. M. McFarquhar, R. M. Rasmussen, L. Xue, C. Liu, and G. Thompson, 2016a: Dynamics of cloud-top generating cells in winter cyclones. Part I: Idealized simulations in the context of field observations. *J. Atmos. Sci.*, **73**, 1507–1527, doi:10.1175/JAS-D-15-0126.1.

——, ——, ——, ——, ——, ——, ——, and ——, 2016b: Dynamics of cloud-top generating cells in winter cyclones. Part II: Radiative and instability forcing. *J. Atmos. Sci.*, **73**, 1529–1553, doi:10.1175/JAS-D-15-0127.1.

Kumjian, M. R., S. A. Rutledge, R. M. Rasmussen, P. C. Kennedy, and M. Dixon, 2014: High-resolution polarimetric radar observations of snow-generating cells. *J. Appl. Meteor. Climatol.*, **53**, 1636–1658, doi:10.1175/JAMC-D-13-0312.1.

Kuo, H. L., 1963: Perturbations of plane Couette flow in stratified fluid and origin of cloud streets. *Phys. Fluids*, **6**, 195–211, doi:10.1063/1.1706719.

Langleben, M. P., 1956: The plan pattern of snow echoes at the generating level. *J. Meteor.*, **13**, 554–560, doi:10.1175/1520-0469(1956)013<0554:TPPOSE>2.0.CO;2.

LeMone, M. A., 1973: The structure and dynamics of horizontal roll vortices in the planetary boundary layer. *J. Atmos. Sci.*, **30**, 1077–1091, doi:10.1175/1520-0469(1973)030<1077:TSADOH>2.0.CO;2.

Luce, H., S. Fukao, F. Dalaudier, and M. Crochet, 2002: Strong mixing events observed near the tropopause with the MU radar and high-resolution balloon techniques. *J. Atmos. Sci.*, **59**, 2885–2896, doi:10.1175/1520-0469(2002)059<2885:SMEONT>2.0.CO;2.

Markowski, P., and Y. Richardson, 2010: *Mesoscale Meteorology in Midlatitudes.* Wiley-Blackwell, 407 pp.

Marshall, J. S., 1953: Precipitation trajectories and patterns. *J. Atmos. Sci.*, **10**, 25–29, doi:10.1175/1520-0469(1953)010<0025:PTAP>2.0.CO;2.

Miura, Y., 1986: Aspect ratios of longitudinal rolls and convection cells observed during cold air outbreaks. *J. Atmos. Sci.*, **43**, 26–39, doi:10.1175/1520-0469(1986)043<0026:AROLRA>2.0.CO;2.

Nicholls, S., 1989: The structure of radiatively driven convection in stratocumulus. *Quart. J. Roy. Meteor. Soc.*, **115**, 487–511, doi:10.1002/qj.49711548704.

Pavelin, E., J. A. Whiteway, R. Busen, and J. Hacker, 2002: Airborne observations of turbulence, mixing, and gravity waves in the tropopause region. *J. Geophys. Res.*, **107**, ACL 8-1–ACL 8-6, doi:10.1029/2001JD000775.

Plummer, D. M., G. M. McFarquhar, R. M. Rauber, B. F. Jewett, and D. C. Leon, 2014: Structure and statistical analysis of the microphysical properties of generating cells in the comma head region of continental winter cyclones. *J. Atmos. Sci.*, **71**, 4181–4203, doi:10.1175/JAS-D-14-0100.1.

——, ——, ——, ——, and ——, 2015: Microphysical properties of convectively generated fall streaks within the stratiform comma head region of continental winter cyclones. *J. Atmos. Sci.*, **72**, 2465–2483, doi:10.1175/JAS-D-14-0354.1.

Rauber, R. M., M. K. Macomber, D. M. Plummer, A. A. Rosenow, G. M. McFarquhar, B. F. Jewett, D. Leon, and J. M. Keeler, 2014a: Finescale radar and airmass structure of the comma head of a continental winter cyclone: The role of three airstreams. *Mon. Wea. Rev.*, **142**, 4207–4229, doi:10.1175/MWR-D-14-00057.1.

——, and Coauthors, 2014b: Stability and charging characteristics of the comma head region of continental winter cyclones. *J. Atmos. Sci.*, **71**, 1559–1582, doi:10.1175/JAS-D-13-0253.1.

——, and Coauthors, 2015: The role of cloud-top generating cells and boundary layer circulations in the fine-scale radar structure of a winter cyclone over the Great Lakes. *Mon. Wea. Rev.*, **143**, 2291–2318, doi:10.1175/MWR-D-14-00350.1.

——, S. M. Ellis, J. Vivekanandan, J. Stith, W.-C. Lee, G. M. McFarquhar, B. F. Jewett, and A. Janiszeski, 2017: Finescale structures of a snowstorm over the northeastern United States: A first look at high-resolution HIAPER Cloud Radar observations. *Bull. Amer. Meteor. Soc.*, **98**, 253–269, doi:10.1175/BAMS-D-15-00180.1.

Rosenow, A. A., D. M. Plummer, R. M. Rauber, G. M. McFarquhar, B. F. Jewett, and D. Leon, 2014: Vertical velocity and physical structure of generating cells and convection in the comma head region of continental winter cyclones. *J. Atmos. Sci.*, **71**, 1538–1558, doi:10.1175/JAS-D-13-0249.1.

Shao, Q., and D. A. Randall, 1996: Closed mesoscale convection driven by cloud-top radiative cooling. *J. Atmos. Sci.*, **53**, 2144–2164, doi:10.1175/1520-0469(1996)053<2144:CMCCDB>2.0.CO;2.

Syrett, W. J., B. A. Albrecht, and E. E. Clothiaux, 1995: Vertical cloud structure in a midlatitude cyclone from a 94-GHz radar. *Mon. Wea. Rev.*, **123**, 3393–3407, doi:10.1175/1520-0493(1995)123<3393:VCSIAM>2.0.CO;2.

Wexler, R., 1955: Radar analysis of precipitation streamers observed 25 February 1954. *J. Atmos. Sci.*, **12**, 391–393, doi:10.1175/1520-0469(1955)012<0391:RAOPSO>2.0.CO;2.

——, and D. Atlas, 1959: Precipitation generating cells. *J. Meteor.*, **16**, 327–332, doi:10.1175/1520-0469(1959)016<0327:PGC>2.0.CO;2.

Wood, R., 2012: Stratocumulus clouds. *Mon. Wea. Rev.*, **140**, 2373–2423, doi:10.1175/MWR-D-11-00121.1.

Yamaguchi, T., and G. Feingold, 2012: Technical note: Large-eddy simulation of cloudy boundary layer with the Advanced Research WRF model. *J. Adv. Model. Earth Syst.*, **4**, M09003, doi:10.1029/2012MS000164.

Young, G. S., D. A. R. Kristovich, M. R. Hjemfelt, and R. C. Foster, 2002: Rolls, streets, waves, and more: A review of quasi-two-dimensional structures in the atmospheric boundary layer. *Bull. Amer. Meteor. Soc.*, **83**, 997–1001, doi:10.1175/1520-0477(2002)083<0997:RSWAMA>2.3.CO;2.